Journal of Alloys and Compounds 1037 (2025) 182503

Contents lists available at ScienceDirect

Journal of Alloys and Compounds

journal homepage: www.elsevier.com/locate/jalcom

Enhanced densification and microstructural refinement in low-Ni WC composites: Conventional sintering optimisation

Aida M. Barja [a,b,*,1], B. Ferrari [b,2], E. Tejado [a,3], J.Y. Pastor [a,4], A.J. Sanchez-Herencia [b,5]

[a] *Departamento de Ciencia de Materiales-CIME, Universidad Politécnica de Madrid, C/ Profesor Aranguren s/n, Madrid 28040, Spain*
[b] *Instituto de Ceramica y Vidrio (ICV), CSIC.C/ Kelsen 5, Madrid 28049, Spain*

ARTICLE INFO

Keywords:
Cemented carbides
Tungsten carbide
Nickel
Vacuum
Sintering
Plasticity
Hardness

ABSTRACT

Nickel is among the substitutes for Co as a binder in cemented carbides due to its higher corrosion resistance, lower cost and critical availability. However, the low wettability of Ni in WC has limited the development of cemented carbides with a low metal binder content, especially when sintered by conventional methods. In this study, high-density WC-Ni cemented carbides, with 10 and 15 Ni vol% (5.9 and 9.1 wt%), were manufactured. To ensure that metal particles were in contact with the WC and thus ensure homogeneous sintering, nanosized-Ni (nNi, from now on) powders were dispersed in a matrix of micron-sized WC powders. Using colloidal processing routes enables high and homogeneous dispersion of nNi throughout the entire volume of the part. Green samples of the two compositions were pressureless sintered under high vacuum and flowing argon atmospheres, both at 1450 ºC and 1500 ºC. The best sintering condition resulted in being under high vacuum at 1450 ºC in terms of microstructural parameters and hardness. Obtaining relative densities of 96.6 % and 97.2 %, WC grain sizes of 2.4 µm and 2.7 µm and Vickers hardness of 10.5 GPa and 9.3 GPa for WC/10Ni and WC/15Ni compositions, respectively. Furthermore, plasticity mechanisms were evaluated by studying the microstructure of the hardness indentation transverse plane.

1. Introduction

The cemented carbide industry is increasingly interested in substituting Co as a binder in WC-based compositions due to two main reasons: the first, which has been considered since 1987 [1] and today is a critical problem [2], is that Co is regarded a strategic material due to its scarcity and increasing demand. Second, the mixture of WC and Co has potential lung toxicity, so sintered WC-Co hard metals were classified as carcinogenic to humans [3,4]. In addition to this, WC-Co presents low corrosion and wear resistance performance under severe working conditions. The leading candidates to replace Co as a binder are Fe and Ni [5] or a combination of both elements, i.e. Fe-Ni [6–8] and Fe-Co-Ni alloys [2,9] also studying de addition of Mo [10]. Iron is beneficial due to its lower price, higher availability and low toxicity, but it has poor corrosion resistance and a poor wettability with WC grains [3], implying higher difficulties during sintering and a low adhesion of the phases. On the contrary, nickel has better wettability than iron with WC grains [3] and excellent corrosion resistance [11], therefore, although other approaches are being investigated, such as WC-W [12] and WC-W_2C [13] compositions for applications where high thermomechanical resistance is needed, or the recent development of HEAs [14] as binder materials, Ni remains as the preferred alternative to Co binder.

To maintain the thermomechanical resistance of the carbide phase, it is necessary to keep the metallic binder additions in the lowest quantity possible but sufficient and homogeneously distributed to have mild sintering conditions to achieve high material densification, i.e. the metallic phase acts as a sintering aid. The colloidal processing technique makes it possible to obtain homogeneous phase distribution [15] of the starting powders even if the quantity of binder is low [5].

In recent years made densification of materials with high melting

---

* Corresponding author at: Departamento de Ciencia de Materiales-CIME, Universidad Politécnica de Madrid, C/ Profesor Aranguren s/n, Madrid 28040, Spain.
E-mail address: aida.martinez.barja@upm.es (A.M. Barja).

[1] ORCID: 0009-0007-5496-1631

[2] ORCID: 0000-0003-3377-6844

[3] ORCID: 0000-0002-5240-6702

[4] ORCID: 0000-0003-3561-5999

[5] ORCID: 0000-0003-2874-6640

https://doi.org/10.1016/j.jallcom.2025.182503
Received 13 June 2025; Received in revised form 22 July 2025; Accepted 23 July 2025

points possible at lower temperatures or in a shorter period. These techniques are known as nonconventional sintering techniques and include spark plasma sintering (SPS), hot isostatic pressing (HIP), hot press sintering (HPS), flash sintering (FS), etc. [16]. These techniques have the disadvantage of being high energy and economically demanding compared to conventional sintering techniques (or pressureless techniques), in which the green body is heated to a defined temperature without applying any external pressure [17]. Besides, nonconventional sintering techniques sometimes have shape and size limitations that make them not applicable in industrial-scale production or in combination with novel manufacturing techniques such as additive manufacturing.

However, due to the difficulties in obtaining full densification, research on WC-based cermets with low Ni binder additions by conventional sintering techniques is still limited [18–21]. Therefore, in this study, the compositions of WC/10Ni and WC/15Ni (in vol%) were formulated by colloidal processing to achieve a homogeneous binder distribution, which makes it possible to act as a sinter-aid even with low Ni amounts. Two sintering atmospheres were studied for both compositions, high vacuum and flowing argon, at two different temperatures: 1450 °C and 1500 °C. A deep analysis of the sintered samples in terms of density, microstructural parameters and hardness was performed to identify the most favourable sintering conditions.

Furthermore, SEM observations of the transverse cross-section beneath the Vickers indentation were conducted to investigate the plasticity mechanisms activated during deformation. This section was accessed using standard grinding and polishing techniques without FIB preparation. It is important to clarify that the use of conventional grinding and polishing techniques to access the indentation cross-section is a well-established method and not introduced as novel in this work. However, although plastic deformation and dislocation behaviour in WC, WC-Co, and WC-Ni systems have been previously examined [22–25], and some studies have analysed transverse sections using FIB-SEM [26,27], detailed microstructural characterisation of the central region beneath the indentation in cemented carbides has rarely been undertaken. In this study, we provide a comprehensive analysis of this region, offering new insights into the local microstructural response without relying on FIB-based preparation.

2. Experimental

2.1. Starting materials and powder mixtures

The starting materials used in this study were two commercially available powders. Tungsten carbide (ST/HT/WC3.5, Wolfram, Austria) with a mean grain size (d_{50}) of 3.4 μm and spherical nanosized nickel particles (UNI 300 CNPC Powder, China) with a mean particle size of 0.3 μm. Two powder mixtures were prepared for this study: WC/10Ni and WC/15Ni, colloidally processed in water, following a procedure described elsewhere [28]. Both mixtures were prepared using high solid content suspensions (31.5 vol%) using deionised water as a dispersion medium and polyethylenimine (PEI Mw-2000, Sigma-Aldrich, Germany) as a dispersant. The detailed powder composition of each mixture is described in Table 1.

The mixture preparation process consists of first adding the Ni powders (minor phase) to deionised water containing the calculated amount of PEI under mechanical stirring, followed by the addition of the WC powders (primary phase). The suspension is ball-milled for one hour at a rotational speed of 250 rpm in a plastic jar. The jar is filled such that one third of its volume is occupied by Si_3N_4 balls, one third by the suspension, and the remaining third by air. Then, the resulting slurries were dried by rotary evaporation under vacuum, and finally, the dried powders were crushed in an agate mortar and sieved.

Table 1
Designation and composition of the cemented carbides studied.

Composition	WC + binder (vol%)		WC + binder (wt%)	
	WC	**Ni**	**WC**	**Ni**
WC/10Ni	90	10	94.1	5.9
WC/15Ni	85	15	90.9	9.1

2.2. Shaping and sintering of the compacts

Conventional shaping and sintering techniques were used to obtain the final compact materials of both compositions, WC/10Ni and WC/15Ni. The compressibility of the granules was measured using a universal testing machine, MicroTest EM2 (MicroTest, Madrid, Spain), applying uniaxial compression stress of up to 240 MPa at a speed of 0.5 mm/min, using a steel die of 5 mm. At the selected pressure, the powders were pressed in the same 5-mm diameter cylindrical steel die, obtaining cylindrical green compacts with an approximate height of 6 mm. The walls of the die and the punches were coated using a mixture of oils (DOSMAR, Spain) as a demolding agent using a brush. The testing machine provides stress and displacement data to construct the pressure–density curves from the compressibility test. The mass and diameter remain constant, while the height at each point is calculated by subtracting the recorded displacement from the initial height. The initial height is the final green compact height plus the total displacement recorded during compression.

Green samples were sintered under different atmospheres and temperatures, as detailed in Table 2, using a tubular furnace with a 99.9 alumina tube (80 mm diameter) under a high vacuum atmosphere (10^{-4} – 10^{-6} mbar) and flowing argon (purity > 99.999 %) atmosphere. Inside the tube, the samples were placed over an alumina crucible, with a sheet of graphite placed at the bottom and the top faces of the sample. Three samples of each sintering condition and composition were manufactured. All sintering trials consist of a single sintering ramp, with a first step of heating from room temperature to the maximum sintering temperature at a heating rate of 5 °C/min, a second step of 1 h to dwell at that temperature, and a final cooling step to room temperature at a cooling rate of 5 °C/min.

2.3. Microstructural, elemental, and mechanical characterisation

The mixed and dried granules of each composition were morphological and elemental characterised by SEM-SE and SEM-EDX, using a field emission scanning electron microscopy (Auriga Series FE-SEM Zeiss, Oberkochen, Germany) with energy dispersive X-ray spectroscopy (EDX, X-Flash detector 5010, Bruker, Germany), applying an

Table 2
Summary of the sintering conditions used and sample designations.

Sample designation	Composition (vol%)	Sintering conditions			
		Atmosphere	Temperature	Dwell	Ramp rate
10Ni-Ar1450	WC/10Ni	Argon	1450 °C	1 h	5 °C/min
10Ni-Ar1500			1500 °C		
10Ni-Vac1450		High vacuum	1450 °C		
10Ni-Vac1500			1500 °C		
15Ni-Ar1450	WC/15Ni	Argon	1450 °C		
15Ni-Ar1500			1500 °C		
15Ni-Vac1450		High vacuum	1450 °C		
15Ni-Vac1500			1500 °C		

operation voltage of 5 kV and 15 kV, respectively.

The density of the green samples was determined geometrically by measuring their height and diameter with a digital caliper with 0.1 mm precision and measuring their mass on the AG245 weighting scale (Mettler Toledo, Swiss) with an accuracy of 0.1 mg. Dilatometric tests of the green samples were carried out to obtain information about the linear contraction behaviour during sintering. It was carried out in a vertical dilatometer with an alumina rod (SETSYS, Setaram, France) under an argon atmosphere, with a heating rate of 5 °C/min up to a maximum temperature of 1500 °C, with a dwell time of one hour.

The density of the sintered samples was measured in ethanol by Archimedes' method according to the ISO 3369: 2006 standard and using the LC-P Density equipment (Mettler Toledo, Switzerland). The relative density of the samples was calculated considering the following theoretical densities of each component: $\rho_{WC} = 15.66 g/cm^3$, $\rho_{Ni} = 8.90 g/cm^3$ and therefore $\rho_{WC/10Ni} = 14.98 g/cm^3$ and $\rho_{WC/15Ni} = 14.65 g/cm^3$.

The samples were cut in its transverse plane and mounted in resin, following the scheme of Figs. 1a and 1b, and then grinded and polished using diamond paste down to one micron. Aluminium foil and carbon adhesive tape made the polymeric resin conductive. In cases where the edges of the sample need to be seen, it was necessary to metallise the sample with carbon using sputtering equipment. The polished samples were chemically etched before microstructural analysis by SEM to reveal the grain boundaries of the WC, using Murakami's reagent: 10 g of $K_3(Fe(CN)_6)$ + 100 ml of distilled water + 10 g of NaOH. The time needed to etch the samples was between 30 and 40 s.

The optical microscope images were obtained with the inverted reflected light microscope Axiovert 100 A (ZEISS, Jena, Germany) on polished and indented samples. The microstructural characterisation was performed on the polished samples by SEM using secondary electrons and an operation voltage of 5 kV, complementarily using EDX with an operation voltage of 15 kV to obtain elemental composition information.

The average grain size, d_{WC}, the grain contiguity of tungsten carbide, C_{WC}, and the mean free path of the nickel binder, λ_{Ni}, were measured on SEM images to characterise the microstructure of the sintered materials; these parameters are related to the mechanical properties of the cemented carbide, and optimising them allows for tailoring the properties of the final material [29,30]. The linear interception method [31] was used to determine the average grain size according to the ASTM E112–13 and UNE-EN ISO 4499–2 standards. Five images of randomly selected areas of each sample, with 10–20 grains in the field of view, were analysed at x2500 magnification for such analysis. In each image, four interception lines were drawn,; at least 50 and 200 grains were intercepted on each image and each sample, respectively.

WC grain contiguity C_{WC} is a quantitative measurement of the degree of mutual contact between grains [32,33], $C_{WC} = 1$ when the carbide grains form a continuous and $C_{WC} = 0$ when the carbide particles are completely isolated between them. In this study, Eq. (1) proposed in [34] was chosen for the calculation of C_{WC}:

$$C_{WC} = 0.036 + 0.973 \bullet \exp\left(-\frac{d_{wc}}{3.901}\right) \bullet \exp\left(-\frac{V_{binder}}{0.249}\right) \tag{1}$$

Here, V_{binder} is the volume of binder present in the cemented carbide. Finally, for the calculation of the mean free path of nickel, Eq. (2) was used [35]:

$$\lambda_{Ni} = \frac{d_{WC}}{1 - V_{Ni}} \bullet \frac{V_{Ni}}{1 - C_{WC}} \tag{2}$$

Where V_{Ni} is the volume of nickel present in the cemented carbide. The mean free path and the contiguity are opposite parameters; hence, a higher mean free path of the binder means that the WCs are spaced between them. The mean free path of the binder was defined as the mean

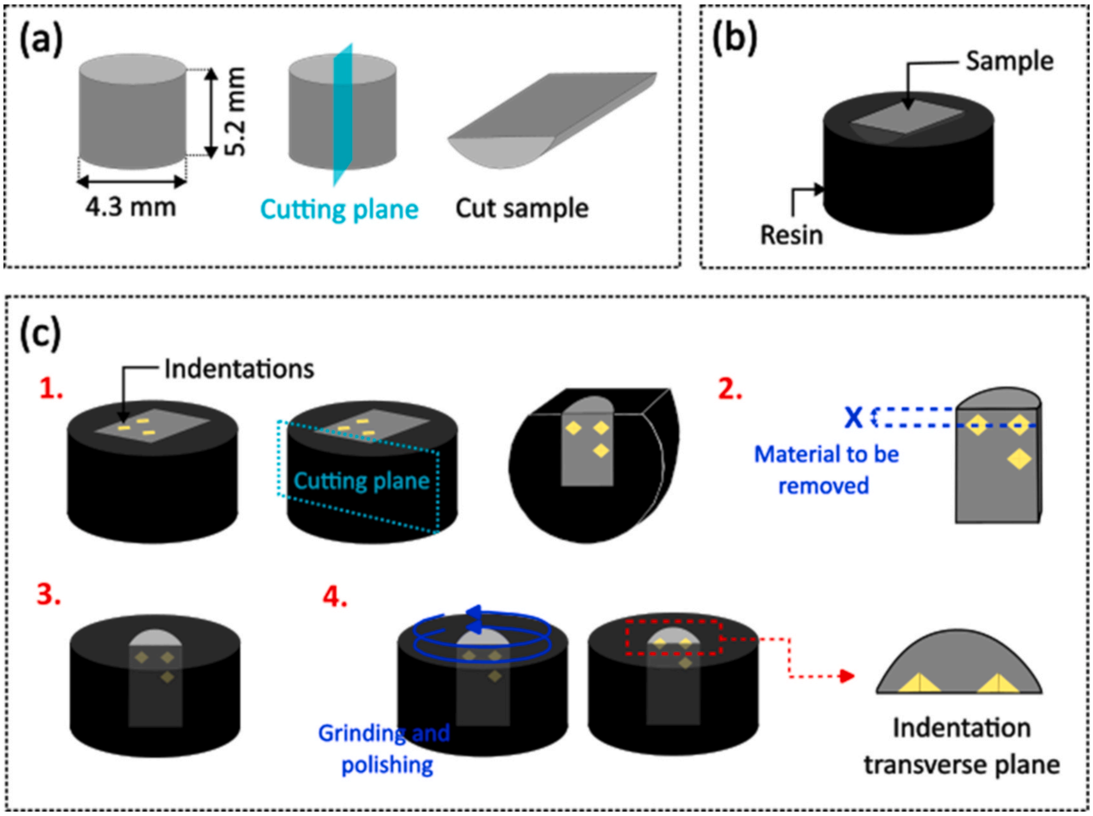

Fig. 1. Scheme of the processes followed for sample preparation. (a) Cut the sample through its transverse section. (b) Sample mounting in the resin. (c) Sample preparation to see the transverse section of the indentation.

size of the metallic phase [36].

The coefficient of variability, *CV(%),* of average grain size, was also calculated with Eq. (3):

$$CV(\%) = \frac{\sigma_{d_{WC}}}{d_{WC}} \bullet 100 \quad (3)$$

where $\sigma_{d_{WC}}$ is the standard deviation, and d_{WC} is the average grain size [37].

Vickers hardness was evaluated on the polished samples with a micro indenter LECO V-100A (LECO, Japan), with loads ranging from 1 kgf (9.8 N) to 50 kgf (490 N), the indentation time was ten seconds in all cases. The diagonals of the indentations were measured with optical microscopy and image analysis software uEye. The equation to calculate the hardness value is Eq. (4):

$$HV = 0.0018544 \quad \times \frac{P}{d^2} \quad (4)$$

Where HV is the hardness in GPa, P is the load applied in N, and d is the mean diagonal length of the indentation in mm.

The procedure for preparing the transverse section at the Vickers indent is illustrated in Fig. 1c. It consists of: 1) cutting the sample near the indentation that is wanted to be seen, 2) measuring with a profile projector the distance from the edge of the sample to the centre of the indentation, 3) mounting the sample in resin again, 4) perform grinding and polishing having into account the removal speed of each grinding step and measure the thickness variation in the profile projector until have removed the necessary quantity to be in the middle of the indentation. The cross-section of the indentations was then analyzed using SEM.

A characteristic defect was found in all samples which was suspected to be graphite. XRD spectra were recorded using an X-ray diffractometer X′Pert MPD (Malvern Panalytical, Malvern, UK), equipped with Cu K_α radiation ($\lambda = 1.540598$ Å). It was operated in the Bragg-Brentano configuration with an angular range of $2\theta = 20–90°$, with step sizes of 0.033° and a time of 100 s / step.

Raman spectroscopy was performed in the graphite type defect regions using the equipment inVia Raman Microscope (RENISHAW, UK), using a $\lambda = 514$ nm and an acquisition time of 10 s.

3. Results and discussion

3.1. Mixed powders characterisation

The morphological and elemental characterisation of the mixed powders by SEM-SE and SEM-EDX is presented in Fig. 2. The SEM images indicate a homogeneous distribution of de Ni particles, which are easily distinguishable from the WC particles due to their spherical shape. Moreover, on the EDX maps (Fig. 2e,f), nickel spherical particles can be identified in blue. This homogeneous distribution of the nNi particles between the micronic WC ones, as a result of the previous colloidal

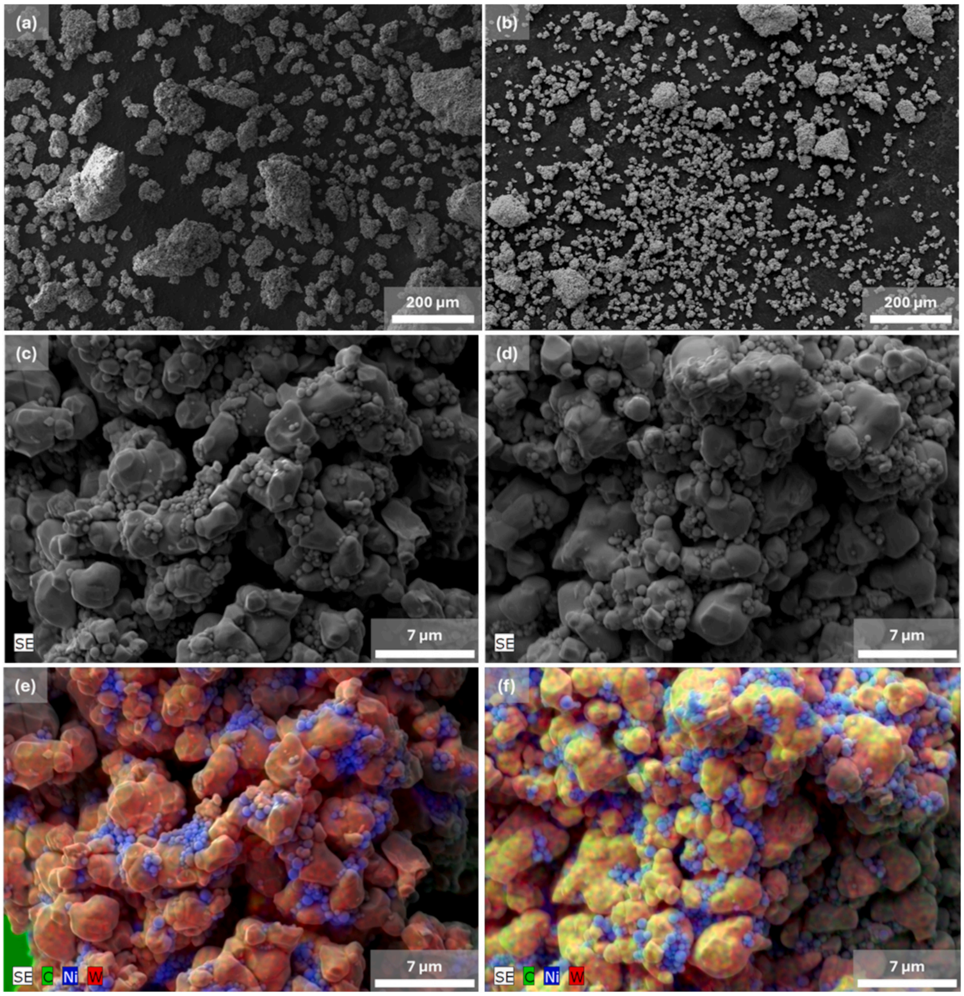

Fig. 2. SEM-SE and SEM-EDX images of mixed WC/10Ni granules (a), (c), (e), and of the WC/15Ni mixed granules (b), (d), (f). Images (a – d) correspond to secondary electron signals at different magnifications, while images (e) and (f) correspond to the elemental composition map obtained with EDX. Carbon is green, nickel is blue, and tungsten is red.

processing of the starting powders, guarantees a homogeneous distribution of the phases in the sintered samples microstructure.

The compressibility curves of the granules are represented in Fig. 3a, where a faster compressibility of the WC/10Ni can be noticed. In both samples, pressure is released as a result of the deformation of the Ni particles. As expected, the lower presence of the metallic phase in WC/10Ni makes the pressure transmit faster than in WC/15Ni. The resulting final relative density is near the same for both powders, around 65 %. Both compositions were uniaxially compressed at 150 MPa to obtain an average green relative density of 64.4 % and 64.2 % with the WC/10Ni and the WC/15Ni mixed powders, respectively. Applying pressures exceeding 150 MPa may lead to the formation of cracks or defects during the demolding of green compacts, due to the strong interactions between the compacted powders and the die walls.

Dilatometry analyses were performed on samples of both compositions to study their shrinking behaviour during sintering, the resulting curves are presented in Fig. 3b. The dilatometry curves are divided into three stages [21], which are represented by green dotted vertical lines in Fig. 3b. Region I corresponds to the pre-initial and initial stages and is where particle rearrangement and neck formation occur through surface transport mechanisms. This stage occurs between 950 – 1305 ºC and 950 – 1280 ºC for WC/10Ni and WC/15Ni, respectively, with a shrinkage of 2.75 % in both cases. The faster ending of that stage for WC/15Ni is justified by its higher binder content, which favours transport mechanisms.

Region II is the intermediate stage, in which the main shrinkage and densification of the sample occur, driven by surface and volumetric transport mechanisms. For both samples, this stage extends up to 1370 ºC with a shrinkage of 10 %. Finally, region III corresponds to the stage where the nickel melts [38]. As the density of molten nickel is lower than the solid one, there is an associated expansion to the melting process, which in the curve means a sudden stop in the shrinkage and even a slight expansion in the WC/15Ni sample. Sintering continues after this temperature by a solution-precipitation mechanism during the dwelling process. The blue arrows in Fig. 3b highlight the shrinkage observed during the dwell time at the highest temperature. It can be seen that the shrinkage rate slows after 30 min, indicating that consolidation has finished and grain growth dominates. At the end of the process, the samples have shrunk by up to 15.1 %, obtaining a relative density of 97.3 % and up to 14.9 %, obtaining a relative density of 97.1 % for the WC/10Ni and the WC/15Ni sample, respectively. The minimal difference between the two compositions does not provide sufficient grounds to conclude that they behave differently.

Given the obtained results, 1450 ºC and 1500 ºC were selected as sintering temperatures, with one hour dwell time. Although sample would continue shrinking if higher dwell times were selected, this would result in larger WC grains [39–41], which is detrimental to some mechanical properties, such as hardness [29,36].

3.2. *Density of the sintered samples*

Three samples were sintered in each atmosphere, and the temperature conditions for both compositions and the average results of their relative density after sintering are presented in Table 3. The samples undergo a shrinkage during sintering of around 13 %. Greater shrinkage was observed during sintering under high-vacuum than argon under otherwise identical sintering conditions and composition.

Compositions with 15 vol% Ni have a higher relative density than those with 10 vol% Ni, this is explained by the liquid phase sintering, where nickel provides both the capillary force and the transport medium to promote densification [40]. Regarding the sintering atmosphere, at 1450 ºC no significant differences were observed. However, at 1500 ºC, a slight increase in density was noted under vacuum conditions for a given composition. This minor increase may be explained by literature on liquid-phase sintering, which reports that vacuum atmospheres facilitate gas removal from pores prior to sintering [39], hence resulting in a higher density after sintering. In contrast, when an inert atmosphere, such as argon, is used, the inert gas inhibits full densification since the trapped argon stabilises closed pores [39]. It is observed that under an argon atmosphere, density unexpectedly decreases when increasing the sintering temperature from 1450 ºC to 1500 ºC. Although no clear explanation for this phenomenon was found, the authors considered that the more pronounced grain growth at 1500 °C may also lead to increased argon entrapment within the sample.

In contrast, samples sintered in a high vacuum atmosphere maintained a constant relative density, or slightly higher, regardless of the sintering temperature. Since sintering at higher temperatures requires more energy and time, resulting in higher costs, the most favourable sintering condition would be under a high vacuum atmosphere at 1450 ºC.

3.3. *Microstructural and elemental characterisation of the sintered samples*

Fig. 4 shows the secondary electron SEM images of the microstructure after chemical etching of WC/10Ni (Fig. 4a-d) and of WC/15Ni (Fig. 4e-h) sintered samples under different conditions. Generally, the WC grains (lighter areas) appear with a polygonal, well-faceted geometry [42], typical of a liquid sintering process, with the nickel (darker regions) located at the triple points or surrounding the grains in a homogeneous and quasi-continuous way. As expected, it appeared in a higher proportion in the 15 vol% Ni samples. The microstructural parameters for all samples are collected in Table 4.

The average WC grain size d_{WC} decreases when sintering under a

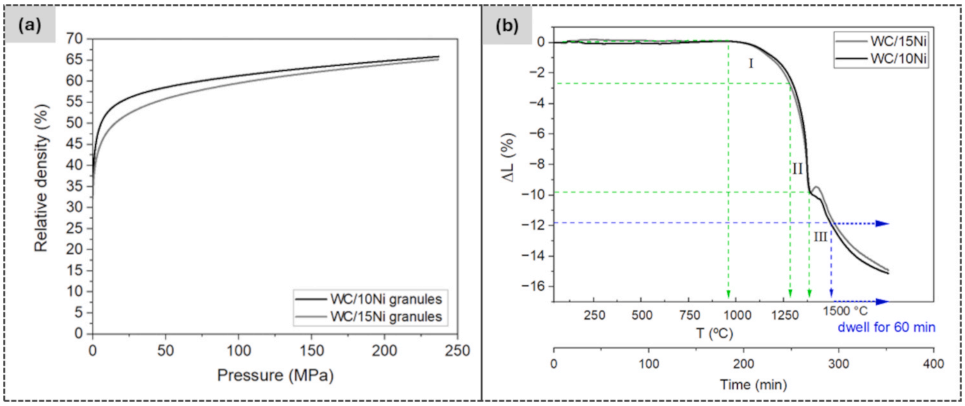

Fig. 3. Mixed powders characterisation. (a) Compressibility curves of the granules. (b) Dilatometric curves of both compositions, pointing out the different stages of the process: I, II and III.

Table 3

Shrinkage and relative density of the samples sintered under different conditions.

Sample	Composition (vol%)	Sintering conditions		Shrinkage (%)*		Relative density ρ (%)*
		Atmosphere	Temperature	Height	Diameter	
10Ni-Ar1450	WC/10Ni	Argon	1450 °C	11.9	13.0	96.50 ± 0.04
10Ni-Ar1500			1500 °C	12.8	12.6	95.58 ± 0.04
10Ni-Vac1450		High vacuum	1450 °C	12.5	13.0	96.63 ± 0.04
10Ni-Vac1500			1500 °C	12.9	12.8	96.7 ± 0.1
15Ni-Ar1450	WC/15Ni	Argon	1450 °C	9.5	12.7	97.24 ± 0.09
15Ni-Ar1500			1500 °C	12.5	13.0	96.47 ± 0.06
15Ni-Vac1450		High vacuum	1450 °C	12.4	13.2	97.20 ± 0.03
15Ni-Vac1500			1500 °C	13.3	13.1	97.16 ± 0.08

* Averaged values for three samples of the same composition

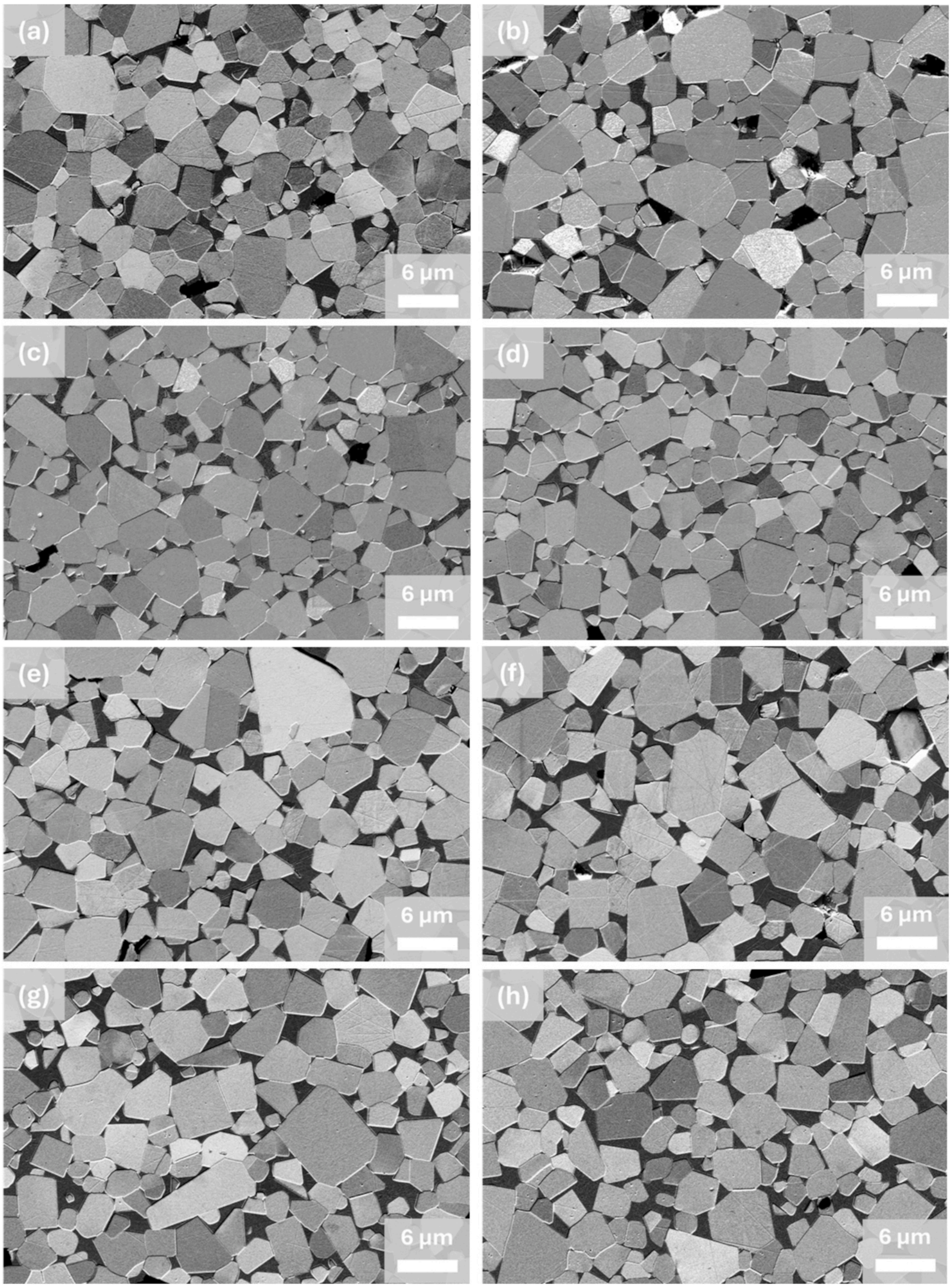

Fig. 4. SEM-SE images of the microstructure after chemical etching of the sintered samples of both compositions and under different sintering conditions. (a) 10Ni-Ar1450. (b) 10Ni-Ar1500. (c) 10Ni-Vac1450. (d) 10Ni-Vac1500. (e) 15Ni-Ar1450. (f) 15Ni-Ar1500. (g) 15Ni-Vac1450. (h) 15Ni-Vac1500. Light areas with polygonal geometries correspond to WC grains, and darker areas correspond to Ni matrix.

Table 4
Microstructural parameters of the sintered samples.

Sintering condition	Argon 1450 °C		Argon 1500 °C		Vacuum 1450 °C		Vacuum 1500 °C	
Sample	**10Ni-Ar1450**	**15Ni-Ar1450**	**10Ni-Ar1500**	**15Ni-Ar1500**	**10Ni-Vac1450**	**15Ni-Vac1450**	**10Ni-Vac1500**	**15Ni-Vac1500**
d_{WC} (μm)	2.5 ± 0.1	2.66 ± 0.07	2.9 ± 0.1	3.3 ± 0.2	2.40 ± 0.07	2.66 ± 0.06	2.49 ± 0.06	2.70 ± 0.08
CV (%)	21.6	12.1	17.9	29.4	13.0	9.7	11.4	14.1
C_{CW}	0.38	0.31	0.34	0.26	0.39	0.31	0.38	0.30
λ_{Ni}	0.45	0.68	0.50	0.80	0.44	0.67	0.45	0.69

high vacuum atmosphere. However, d_{WC} increases when the amount of binder increases and the sintering temperature increases, which correlates with the literature [41]. This is due to the lower viscosity of the molten nickel at 1500 °C [43] which favours the liquid phase migration (LPM) [44] during the solution-precipitation process. The increase in d_{WC} with a higher binder content could be related to the solution precipitation phenomena of the WC grains in the Ni liquid phase. The carbide grain contiguity C_{CW} decreases with a larger amount of binder, while the mean free path of binder λ_{Ni} increases, as expected [36,39,41] because there is a higher probability that the binder phase surrounding

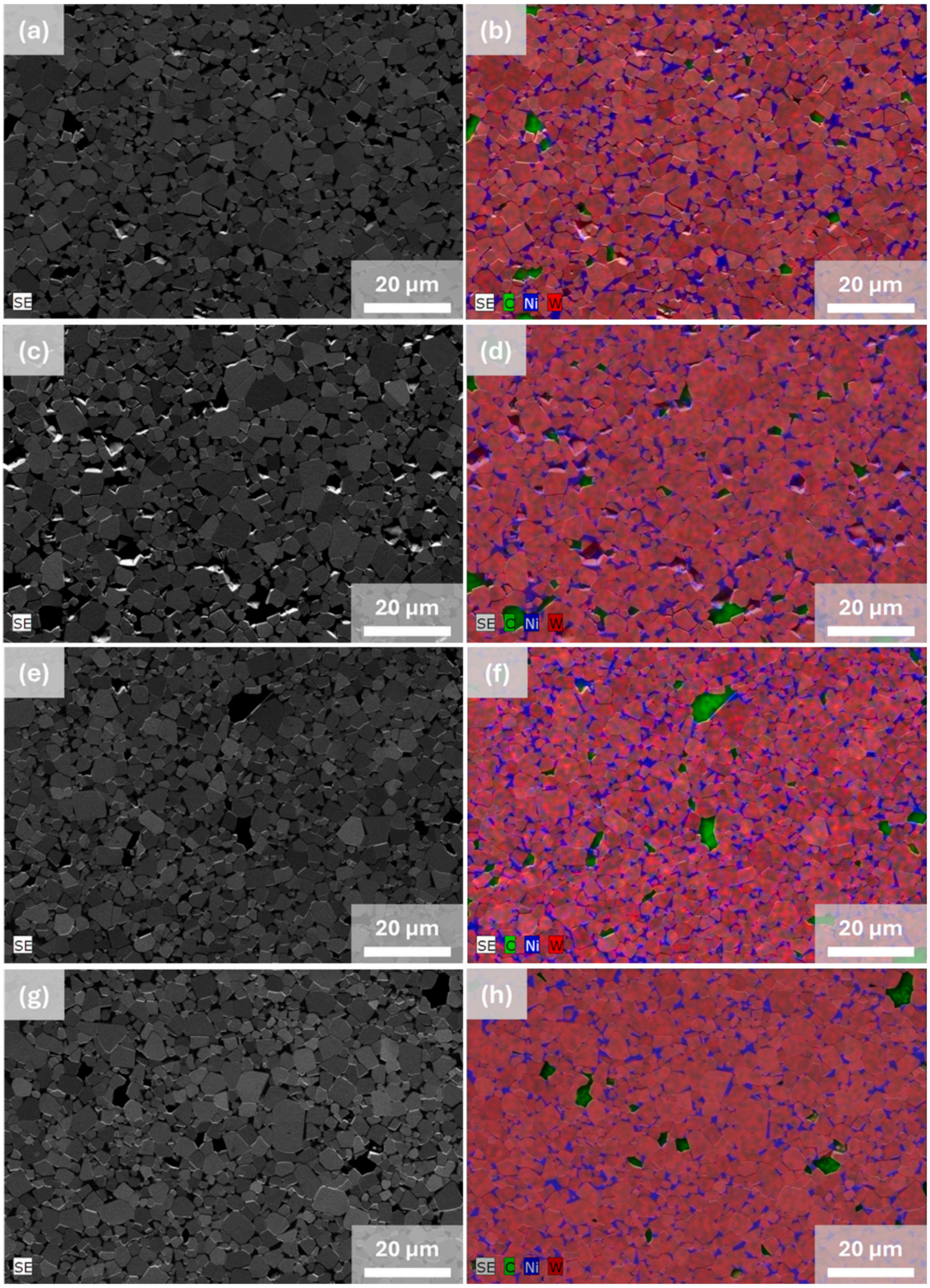

Fig. 5. SEM-EDX elemental map of the sintered WC/10Ni simples. (a-b) 10Ni-Ar1450. (c-d) 10Ni-Ar1500. (e-f) 10Ni-Vac1450. (g-h) 10Ni-Vac1500. The secondary electron images are shown in the left column and the composition maps obtained by EDX are shown in the right column.

the carbide particles.

In the same way, C_{CW} decreases (and λ_{Ni} increases) when increasing the sintering temperature, as described in [41]. Finally, sintering in a high vacuum results in higher C_{CW} and lower λ_{Ni} than in an argon atmosphere. It is difficult to conclude the coefficient of variability of the carbide grain size *CV(%)*. It can be noticed that when sintering at 1450 ºC is higher for the 10 vol% Ni compositions, and when sintering at 1500 ºC is higher for the 15 vol% Ni ones. The most important fact is that *CV (%)* decreases when sintering using a high vacuum atmosphere, resulting in a more homogeneous microstructure. Therefore, the most beneficial sintering condition is under a vacuum atmosphere at 1450 °C to obtain a homogeneous microstructure with a small grain size.

The elemental maps are presented in Fig. 5 and Fig. 6 for the samples of WC/10Ni and WC/15Ni compositions, respectively. With respect to the colour map, tungsten is red, carbon is green, and nickel is blue. The homogeneous distribution of the nickel matrix between the tungsten carbide grains can be appreciated.

Two defects can be identified in the microstructure, independently of the composition and sintering method used. For this reason, they will be exemplified in randomly selected samples, Fig. 7. The material pull-out defect is highlighted in Fig. 7a, and it is caused during the sample preparation processes: cutting, grinding, and polishing. Fig. 7b shows a defect suspected of being graphite, as in previous studies [5]. Analysing the W-C-Ni diagram [19,38] graphite may precipitate during cooling if the carbon content exceeds the small carbon window for stoichiometric WC formation (between 5.2 % and 5.45 %C in WC – 10 wt% Ni compositions [38]). This excess of graphite could result from compositional changes caused by the graphite foils placed at the top and the bottom of

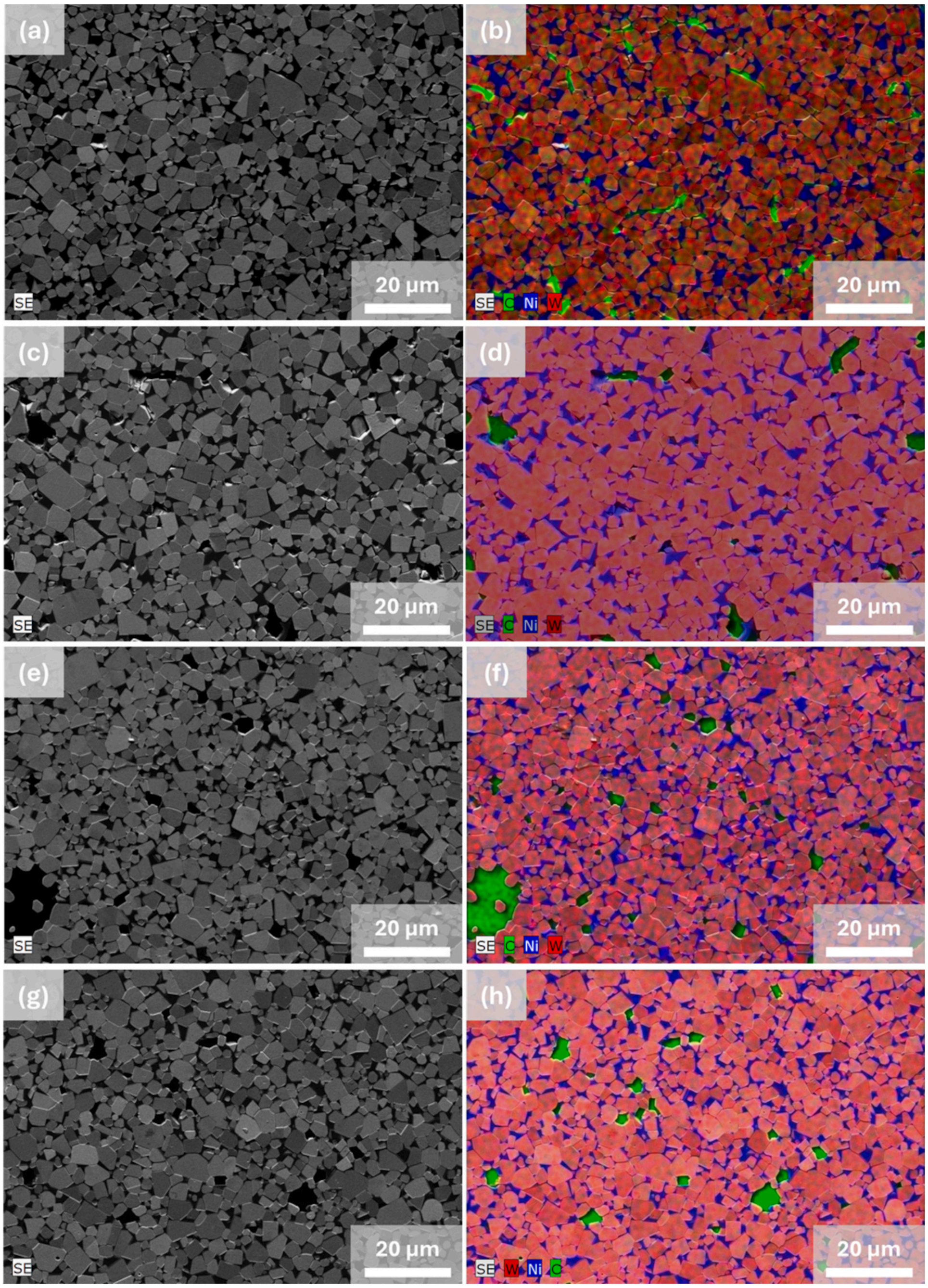

Fig. 6. SEM-EDX elemental map of the WC/15Ni sintered simples. (a-b) 15Ni-Ar1450. (c-d) 15Ni-Ar1500. (e-f) 15Ni-Vac1450. (g-h) 15Ni-Vac1500. The secondary electron images are shown in the left column and the composition maps obtained by EDX are shown in the right column.

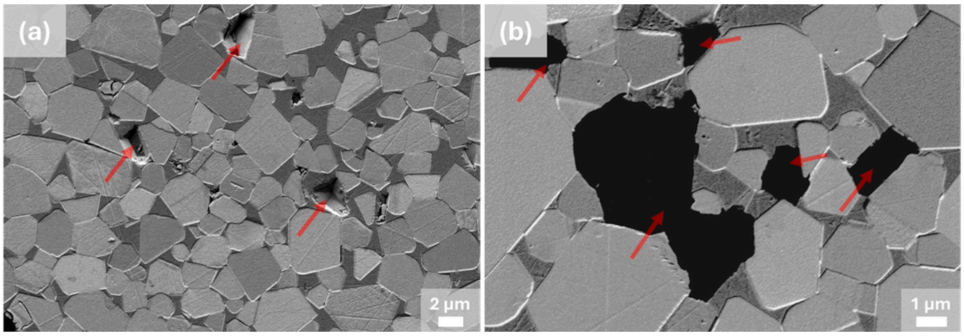

Fig. 7. SEM-SE images of the two common defect types highlighted by red arrows: (a) material pull-out and (b) graphite.

the sample during sintering, as well as residues of the dispersant (PEI) in the powder mixture.

The presence of graphite was further analysed by SEM-EDX, X-ray diffraction and Raman spectroscopy, as shown in Fig. 8. The tungsten carbide signal was identified based on PDF-file 51–0939 ICDD, while nickel was detected according to [45], graphite signal was plotted with data retrieved from PDF-file 41–1487 ICDD. While XRD analysis, shown in Fig. 8c, did not addressed the presence of graphite (indicated in blue in the XRD spectrum), its presence could be clearly distinguished from particles pulled-out from the surface in the EDX mapping of carbon (Fig. 8b).

In order to identify the allotropic form of carbon present in the material, Raman spectroscopy was performed on a graphite-type defect area (Fig. 8e); the graphite spectrum obtained is shown in Fig. 8d. The analysis was carried out on a WC/10Ni sample, selecting different regions. First, the objective was to discard the possibility of this defect being a hole or pore in which the polishing diamond suspension was retained, however, the Raman spectra of diamond has only a very intense peak at 1332 cm^{-1} [46–49], which was not present in the spectra. Another possibility would be to have amorphous carbon, but the spectrum obtained does not match the variations given in [47,48] or [50]. This latter presents an amorphous carbon spectrum with two peaks but with a FWHM wider than in this study: the first one in the range of 1320–1360 cm^{-1}, and the second peak ranging from 1500 to 1600 cm^{-1}. Therefore, the possibility of having amorphous carbon was discarded. Finally, it was concluded to be graphite because the peaks D at 1360 cm^{-1}, G at 1583 cm^{-1} and the 2D band at 2721 cm^{-1} match with the results for graphite obtained in [46–51]. In the case of graphene, the peaks are in the same position, but the difference is that the 2D peak is more intense than the G peak [51]. However, in this study, the G peak is more intense than the 2D peak.

Ni segregations were found at the edges of the sample in all the samples sintered under an argon atmosphere, Fig. 9. They were identified by SEM (Fig. 9a), verifying by EDX that the segregation composition was nickel, coloured in blue (Fig. 9b). These segregations are not beneficial because they mean that the Ni is not inside generating a compact microstructure, and it may result negatively with regard to mechanical properties, supporting the fact that it is more advantageous to sinter in a high-vacuum atmosphere.

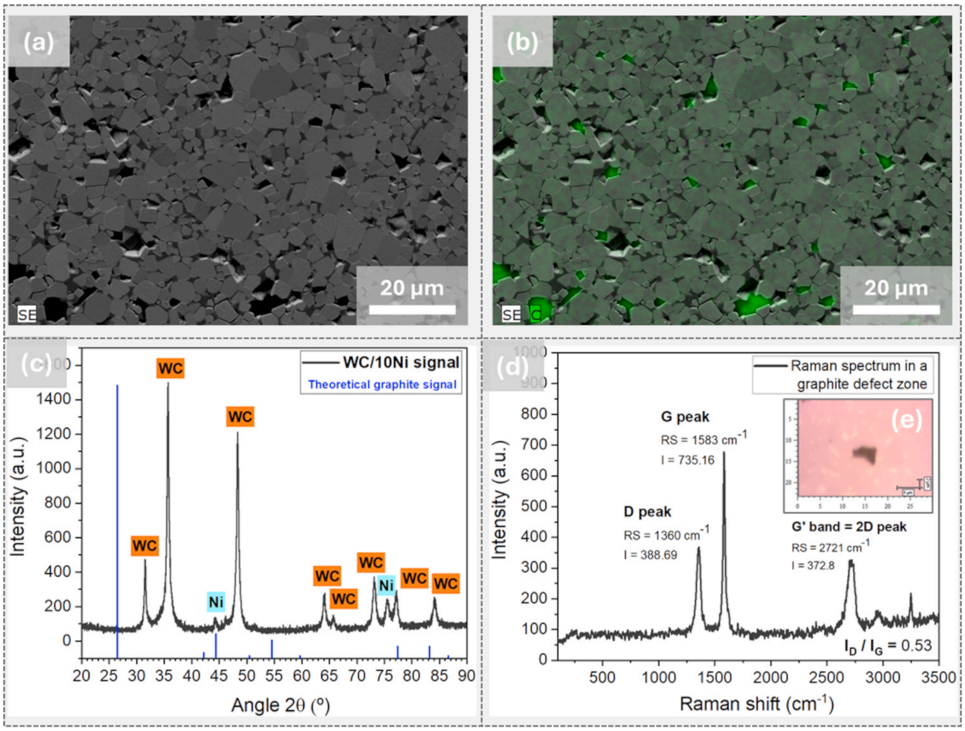

Fig. 8. Graphite type defect characterisation: (a-b) SEM-EDX images with a mapping of carbon (in green), which is noticeable in the differences between pulled-out particles and graphite type defects, (c) DRX spectrum. The blue lines represent the peaks that would have corresponded to graphite. WC and Ni signals were obtained and pointed out over the peaks. (d) Raman spectrum of a graphite-type defect. as highlighted in (e).

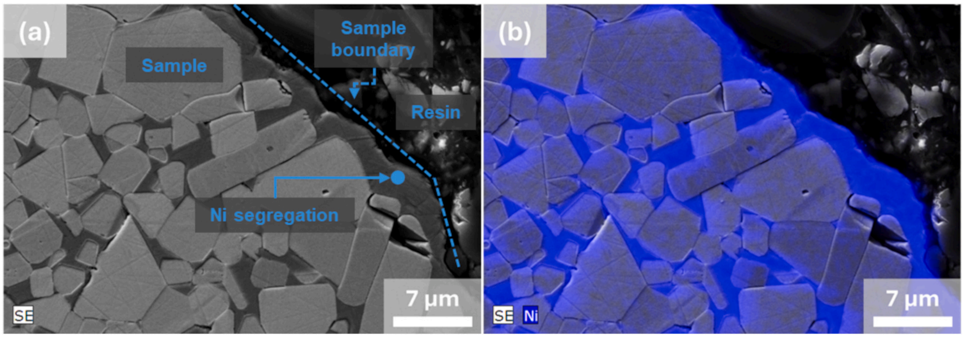

Fig. 9. Ni segregations on the sample edge when sintering under an argon atmosphere. (a) SEM-SE image of the segregations, and (b) SEM-EDX image of the composition map colouring Ni in blue. The original version of this image, without labels, is available as Fig. S1 in the Supplementary Material.

3.4. *Mechanical characterisation of the sintered samples*

Hardness was measured in all the samples, applying a load of 9.8 N, while hardness of specimens sintered at 1450 ºC was also evaluated with indentation loads ranging from 49 N (5 kgf) to 490 N (50 kgf). Fig. 10a shows the hardness values measured for all the sintered materials, it can be seen that the difference in hardness directly correlate with the Ni content, but also with differences in grain size. A small grain size results in a more rigid material. Therefore, the samples sintered under a vacuum atmosphere are harder than those sintered under an argon atmosphere. As well as the samples sintered at 1450 ºC regarding to those sintered at 1500 ºC. Samples with 15 vol% Ni are always less hard than those with 10 vol% Ni. In addition to being related to a larger grain size, this is also due to the higher quantity of soft phase (nickel phase) in the microstructure. This is also reflected in a higher λ_{Ni} and a lower C_{CW}, which results in a lower hardness but an expected higher toughness [22, 36]. Based on the results obtained, it was concluded that sintering under a vacuum atmosphere at 1450 °C is the most appropriate sintering condition to improve the hardness of the material.

The influence of the load applied on the hardness results obtained was also studied for the samples sintered at 1450 ºC, using an indention load of 49 N (5 kgf), 98 N (10 kgf), 196 N (20 kgf), 294 N (30 kgf) and 490 N (50 kgf), as shown in Fig. 10b. This selection was based on the best characteristics shown in microstructure and hardness when compared with the samples sintered at 1500 ºC. Fig. 10b shows how hardness decreases when the load applied up to a value of 98 N. Even if the load increases, the hardness values remain pretty constant compared to that value. This happens because the diagonal indentation length increases as load increases, covering a larger microstructure area with more WC grains, Ni matrix and defects, resulting in a more representative average of the material's hardness. This is reflected in decrease in the measurement error when indenting at higher loads. The Vickers indentation should be performed with a minimum load of 98 N to obtain a reliable value of the hardness of these materials. An exception to this behaviour was found in sample 10Ni-Ar1450, and it may be related to a more heterogeneous distribution of defects in this sample surface. The average hardness of these materials, measured with 490 N load, resulted in 8.81 ± 0.07 GPa, 10.49 ± 0.08 GPa for WC/10 Ni samples sintered under argon and vacuum, respectively; and 8.4 ± 0.1 GPa and 9.30 ± 0.08 GPa for WC/15Ni samples sintered under argon and vacuum, respectively.

Some trials were performed to measure fracture toughness by indentation, but even when indenting the sample the maxium load (490 N, 50 kgf), cracks did not appear in all the indentation vertices, which means that the materials showed a strong plastic behaviour [43]. Examples of the hardest (Fig. 11a) and the softest (Fig. 11b) material indented with 490 N are shown. It would be expected that the hardest material would have a more brittle behaviour and produce these cracks, but this did not happen in this study, indicating that the manufactured materials have a high fracture toughness.

3.5. *Study of the plasticity mechanisms*

The impossibility of measuring fracture toughness via indentation, as well as the low hardness obtained in comparison with the previous studies of compositions of WC cermets with low Ni content as a binder [5,6,18,52–55], denotes the presence of an important plasticity mechanism preventing crack formation, which results in a high toughness. To study this plasticity mechanism, hardness indentations were observed in the basal and transverse planes by SEM-SE and SEM-EDX techniques. To facilitate a better understanding of the observed indentation planes, a schematic representation is provided in Fig. 12.

In the SEM-SE images of the basal plane, Fig. 13, different indentation regions are signaled with red arrows and numbers and then included at higher magnifications. Relevant fracture and deformation mechanism are labelled and signaled over the images with white arrows.

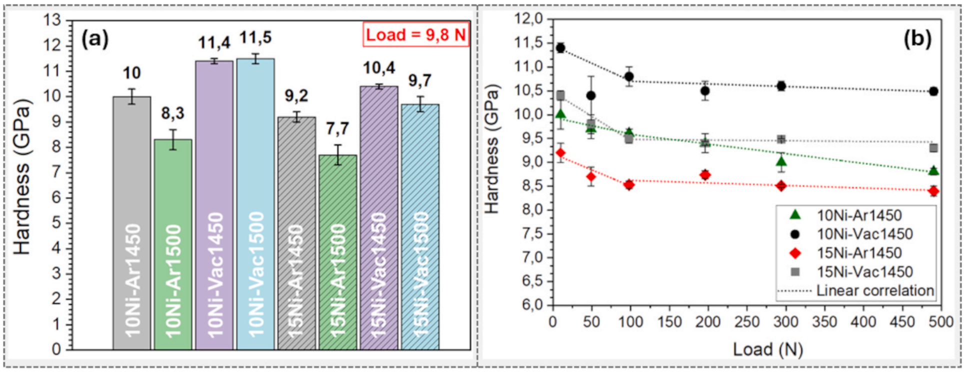

Fig. 10. Vickers hardness results. (a) Results for the indentations of 9.8 N that were performed in all the samples. (b) Load vs hardness results for the samples sintered at 1450 ºC. The dotted lines correspond to the linear correlations.

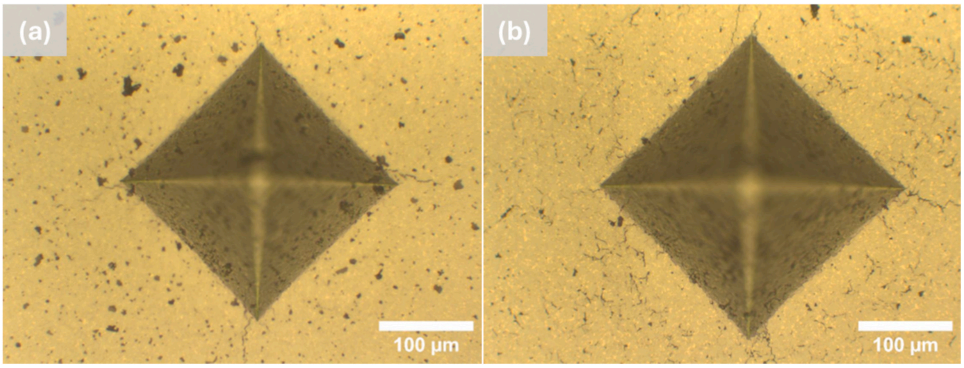

Fig. 11. Optical microscope images of Vickers indentations performed at 490 N. No cracks from the four vertex that allow fracture toughness calculation were present. Examples are (a) the hardest sample, 10Ni-Vac1450, and (b) softest sample, 15Ni-Ar1450.

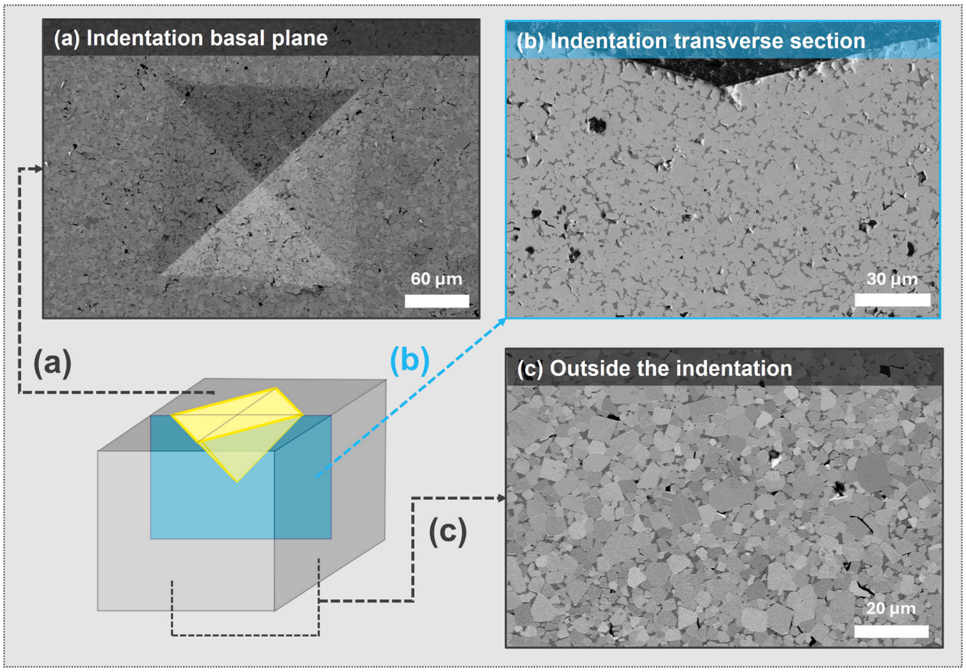

Fig. 12. Scheme of the different indentation sections studied by SEM.

The fracture toughness of cemented carbides is described as a two-step process: a brittle intercrystalline and transcrystalline fracture of the carbide phase, followed by ductile rupture of the binder phase and the carbide-binder interfaces [56]. In Fig. 13, region number 2, a brittle intercrystalline fracture of the carbide followed by ductile rupture of the carbide-binder interfaces occurred. No ductile fracture of the binder phase is observed. However, the plastic deformation of the nickel matrix allows for the rearrangement of the carbide grains. The latter can be seen very clearly in the deformation region number 4, where the carbide grains have been stacking due to the plasticity of the nickel matrix, which has been repositioned to allow it. Also, in region number 3, a critical WC carbide grains rearrangement is appreciated if we focus on the areas where a higher concentration of nickel is seen concerning the rest of the microstructure. Examples of transcrystalline brittle fracture can be found in regions 1, 3 and 4, where some WC grains show cracks through them. Furthermore, WC has been reported to undergo a high level of plastic deformation by dislocation movement and not only by grain boundary sliding [23]. In some of the grains, we can observe beach marks indicating the direction of deformation through the grain.

Elemental EDX maps of different indentation deformation regions are included in Fig. 14 to easily appreciate the plasticity of the nickel matrix that allows the carbide grain rearrangement stated previously.

Furthermore, the transverse section of the indentation was observed by SEM-SE, Fig. 15 and SEM-EDX, Fig. 16, to check how the plasticity mechanisms occur on the sides and under the indentation. Figs. 15a and 15b show two different indentations. For each indentation, three distinct areas were selected for analysis: Area 1 corresponds to the microstructure beneath the indentation, while Areas 2 and 3 refer to the microstructure on either side of the indentation. These regions are examined at higher magnification in Fig. 15c–h. In the images, selected zones representing deformation of the nickel matrix - facilitating the movement of WC grains - are outlined in yellow. Additionally, regions indicating significant rearrangement of WC grains are marked in purple. In contrast with indentation basal plane images, no evidence of brittle intergranular or transgranular fracture across the WC grains is observed, nor are any cracks present. This suggests that ductile plastic deformation mechanisms are predominant in this region, primarily involving the Ni matrix.

The EDX colour map presented in Fig. 16 facilitates the identification of the deformation mechanisms occurring in the nickel matrix, as discussed above.

In view that no cracks were observed either from the vertex of the

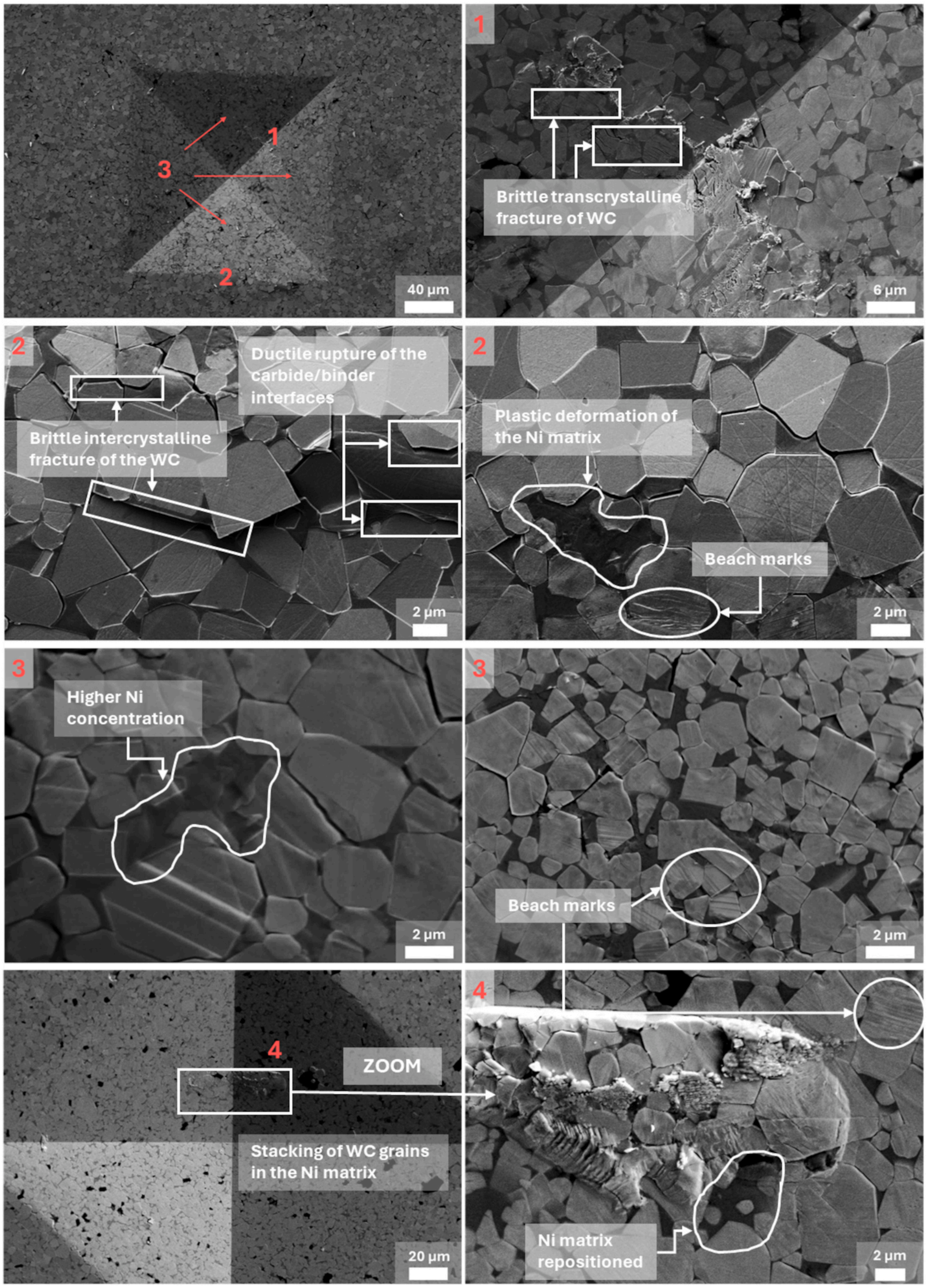

Fig. 13. SEM-SE images of the indentation basal plane. Indentation areas are differentiated with red numbers and arrows, also included at higher magnifications. Interesting fracture and deformation features are labelled over the images and signalled with white arrows. The original version of this image, without labels, is available as Fig. S2 in the Supplementary Material.

basal plane indentation or in the region beneath it, and considering that the dominant deformation mechanism involved ductile rearrangement of the Ni matrix to accommodate WC grain repositioning, it can be concluded that the materials produced in this study exhibit high toughness, despite the low content of soft phase (5.9 and 9.1 wt% Ni). This behaviour is attributed to the homogeneous distribution of the binder around the carbide particles, achieved through the colloidal processing route. The plasticity mechanisms responsible for impeding crack propagation during indentation are primarily governed by the local rearrangement of WC grains within the Ni matrix.

3.6. *Discussion of results*

Table 5 summarises previous studies about WC-based cemented carbides with low Ni content as the binder phase. It can be noticed that little research has been published on compositions with as low quantities of Ni as in this study, i.e. 5.9 wt%. Furthermore, focusing on conventional sintering, only one work uses a lower amount of binder. The relative density value obtained is in the range of the literature results, only overpassed when higher quantities of binder or non-conventional sintering routes are used. Material densification is greater under non-conventional sintering due to the applied pressure, which promotes earlier liquid phase formation and enhances solution–precipitation mechanisms. Additionally, pressure aids in gas elimination, reducing

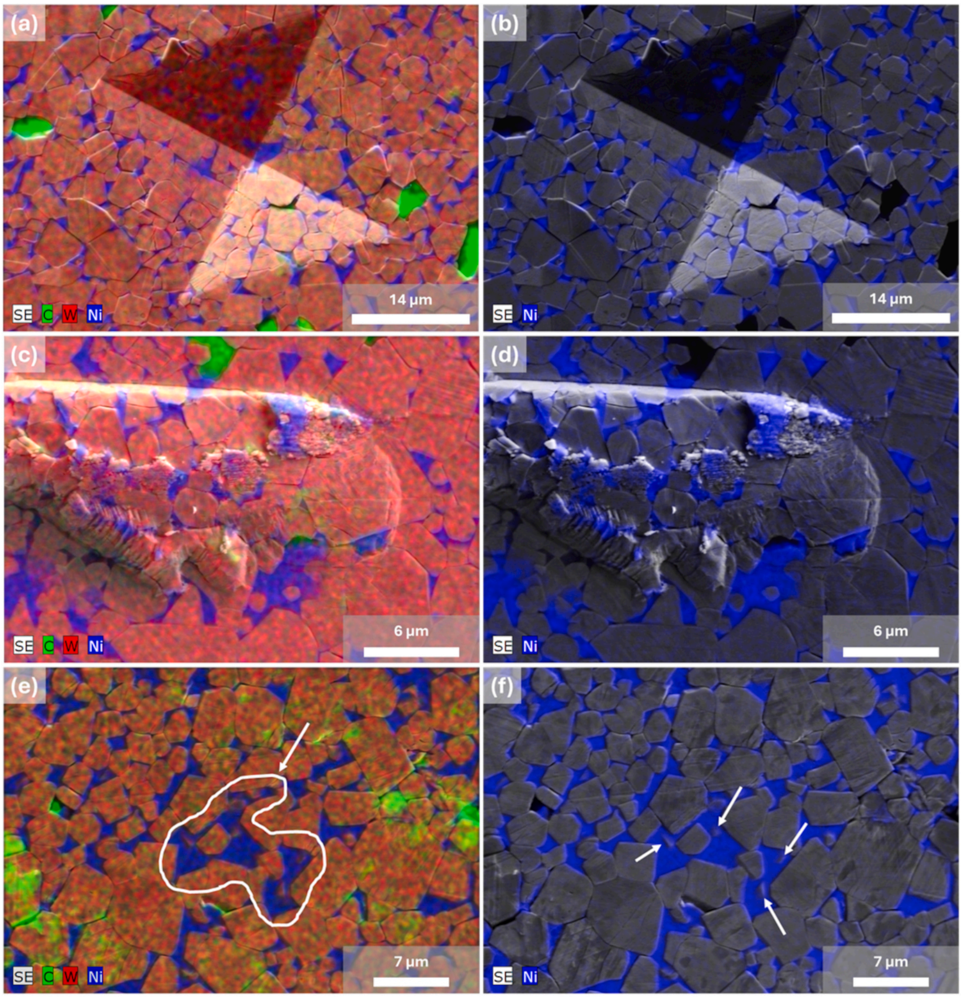

Fig. 14. SEM-EDX compositional maps of different indentation regions. (a-b) Complete indentation view. (c-d) Important carbide grain stacking region. (e) Important nickel matrix concentration region, highlighting with white arrows (f) WC grains rotated inside the matrix.

porosity and improving overall densification.

Regarding grain size, only one study employing conventional sintering assessed this parameter, reporting larger grain sizes than those observed in the present work, which correlates with lower hardness. This difference may also be attributed to the higher binder content. Grain size tends to be smaller when non-conventional sintering techniques are employed, primarily due to the typically faster processing conditions. These methods often involve higher heating rates and significantly shorter dwell times at the maximum temperature — for instance, in spark plasma sintering (SPS), the holding time is commonly limited to around 10 min. Such conditions limit grain growth, resulting in finer microstructures.

Drawing direct comparisons in terms of hardness is challenging, as it is strongly influenced by the binder content, which varies across all cases. Hardness is also affected by the final density. Although densities exceeding 96 % were achieved in the samples analysed in the present study, the remaining internal porosity corresponds to very small pores homogeneously distributed throughout the sample volume. Optical micrographs at lower magnifications for the 10Ni-Vac1450 and 15Ni-Vac1450 samples are provided in Figure S4 of the Supplementary Material, where these small pores can be observed. In conventional sintering, higher nickel content generally leads to increased densification and, consequently, greater hardness. However, a higher metallic binder content also implies a greater proportion of soft phase, which in turn leads to a reduction in hardness. This occurs, for instance, in [18], where a hardness of 13.23 GPa was reported for an alloy with 8 wt% Ni, higher than the 9.3 GPa measured in this study for 9.1 wt% Ni. This discrepancy may be attributed to the higher relative density in [18] (99.8 % vs. 97.2 %), as well as the slightly lower Ni content. However, higher hardness was obtained compared to [20], which can be attributed to the significantly higher binder content in that study (20 wt%). Similarly, in [21], a markedly lower hardness was reported despite a comparable Ni content (5 wt%).

Besides, in non-conventional sintering, the higher density achieved — due to the mechanisms previously discussed — combined with the finer grain size, contributes to the observed increase in hardness. Therefore, the hardness value obtained in this study falls within the expected range, considering the sintering route and the amount of binder added.

4. Conclusions

WC-based cemented carbides with low Ni contents (10 and 15 vol%) were successfully fabricated via conventional sintering, achieving a homogeneous binder distribution through prior colloidal powder processing.

Sintering conditions were carefully optimised to enhance densification, microstructural features, and mechanical properties. Two sintering atmospheres - high vacuum and argon - were compared at 1450 °C and 1500 °C. Vacuum sintering slightly improved densification in some cases by facilitating gas evacuation from pores, and results in a smaller d_{WC}, leading to increased hardness. Under argon sintering, *CV(%)* increased,

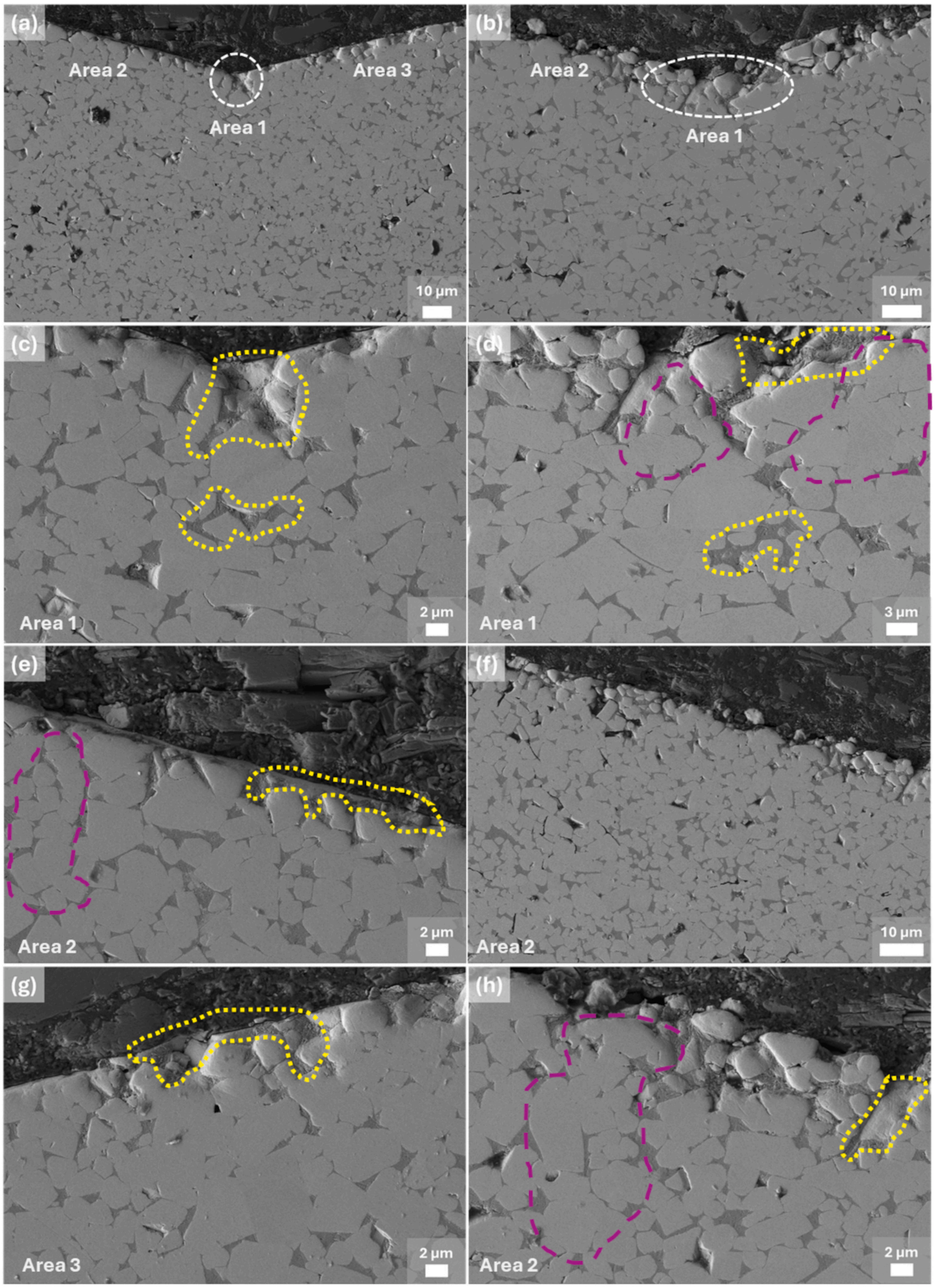

Fig. 15. SEM-SE images of the transverse section of two Vickers indentations (a, c, e and g) and (b, d, f and h). Relevant regions of Ni matrix deformation are highlighted in yellow, while examples of significant WC grain rearrangement or pile-up zones are indicated in purple. The original version of this image, without labels, is available as Fig. S3 in the Supplementary Material.

indicating greater microstructural heterogeneity, and Ni segregation was detected at sample edges. No significant differences were observed between the two sintering temperatures.

After comparing the obtained results, it was concluded that sintering under a high vacuum atmosphere at 1450 °C is the most beneficial for grain size and hardness. Obtaining the best results of 96.6 % and 97.2 % relative density, 2.4 μm and 2.7 μm of WC grain size and 10.5 GPa and 9.3 GPa of Vickers hardness for the WC/10Ni and WC/15Ni compositions, respectively.

Furthermore, the plasticity mechanisms in these materials were investigated through microstructural observations of the central cross-section beneath the Vickers indentation. This represents a significant contribution of the present study, as such detailed imaging of this specific region has not been previously reported in the literature on cemented carbides.

CRediT authorship contribution statement

E. Tejado: Writing – review & editing, Supervision, Project administration. **B. Ferrari:** Supervision, Methodology. **Aida M. Barja:** Writing – review & editing, Writing – original draft, Investigation, Formal analysis. **A.J. Sanchez-Herencia:** Writing – review & editing, Supervision, Project administration, Methodology, Formal analysis. **J.Y. Pastor:** Writing – review & editing, Supervision, Methodology.

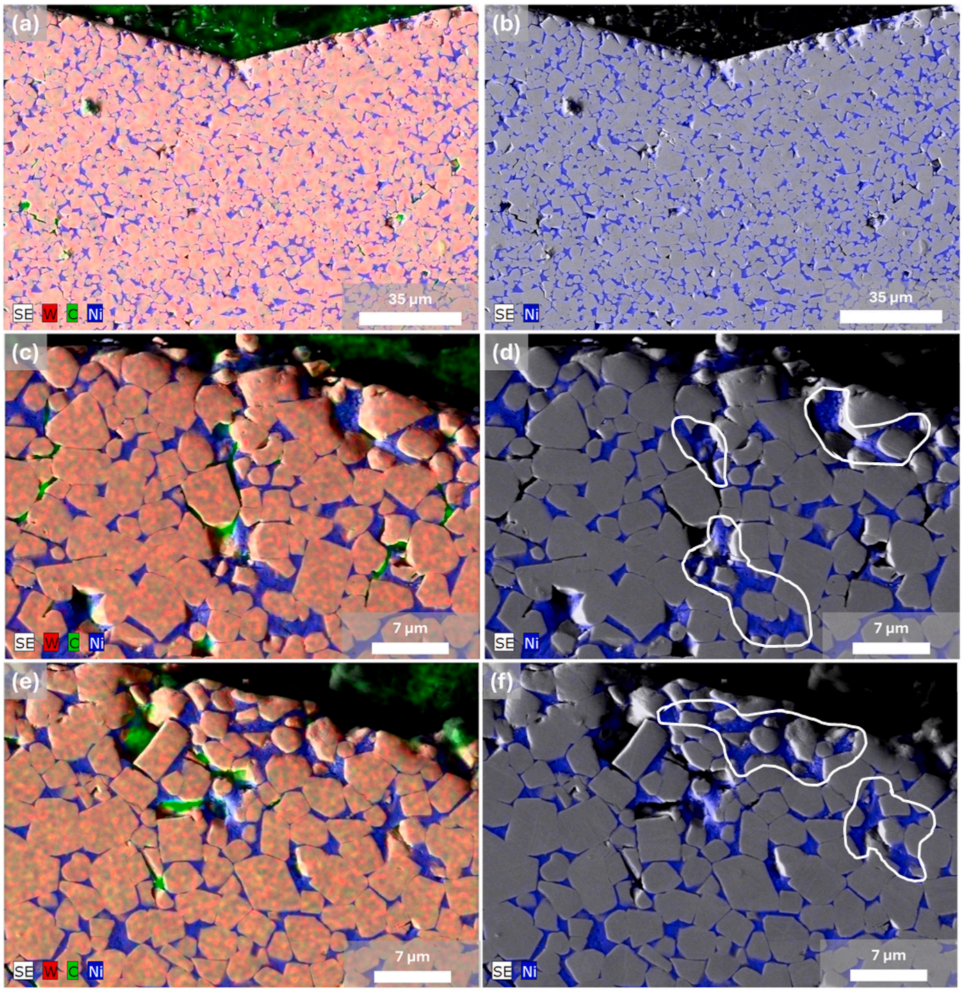

Fig. 16. SEM-EDX images of the Vickers indentation transversal plane. Examples of regions exhibiting significant deformation of the Ni matrix, enabling WC grain rearrangement, are indicated in white.

Table 5
Summary of previous research on WC-based cemented carbides with low Ni addition: comparison of WC grain size, relative density and Vickers hardness.

Reference	Composition	Processing	dwc (µm)	Density (%)	HV (GPa)
This study	**WC + 5.9 wt% Ni**	**Conventional:** Vacuum sintering at 1450 ºC	2.40 ± 0.07	96.63 ± 0.04	10.49 ± 0.08
This study	**WC + 9.1 wt% Ni**	**Conventional:** Vacuum sintering at 1450 ºC	2.66 ± 0.06	97.2 ± 0.03	9.30 ± 0.08
[18] Phuong et al. (2016)	**WC + 8 wt% Ni**	**Conventional:** Vacuum sintering at 1450 ºC	-	99.8	13.23
[19] Wen et al. (2023)	**WC + 10 wt% Ni** + 2.5 wt% W	**Conventional:** N2 sintering at 1480 ºC	-	98.5	-
[20] Steinlechner et al. (2021)	**WC + 20 wt% Ni** + 4.3 wt% C	**Conventional:** Vacuum sintering	3.6	-	6.8
[21] Lima et al. (2024)	**WC + 5 wt% Ni**	**Conventional:** Vacuum sintering	-	91.8	7
[5] Garcia-Ayala et al. (2021)	**WC + 3 wt% Ni**	NON-Conventional: HPS	2.9	98.3	19.5 ± 0.5
[52] Zegai et al. (2023)	**WC + 10 vol% (W+5vol%Ni)**	NON-Conventional: SPS	-	99.8	18.9 ± 0.3
[53] Rong et al. (2012)	**WC + 6 wt% Ni**	NON-Conventional: SPS	-	92.3 ± 0.2	24 ± 0.5
[54] Kim et al. (2015)	**WC + 3 wt% Ni**	NON-Conventional: SPS	0.3	99.6	22
[57] Shi et al. (2015)	**WC + 8 wt% Ni**	NON-Conventional: HIP	-	-	-
[55] Ghasali et al. (2017)	**WC + 10 wt% Ni**	NON-Conventional: SPS	-	99.9	17.8 ± 0.4

Declaration of Competing Interest

The authors declare the following financial interests/personal relationships which may be considered as potential competing interests: Aida M. Barja reports financial support was provided by State Agency of Research. E. Tejado reports financial support was provided by State Agency of Research. A.J. Sanchez-Herencia reports financial support was provided by State Agency of Research. If there are other authors, they declare that they have no known competing financial interests or personal relationships that could have appeared to influence the work reported in this paper.

Acknowledgements

This work is part of the Projects PID2022–137274NB-C31 and PID2022–137274NB-C33 funded by MICIU/AEI/10.13039/501100011033 and FEDER, UE. First author acknowledges financial support through the grant PREP2022–000139 funded by MICIU/AEI/10.13039/501100011033 and FSE+.

Appendix A. Supporting information

Supplementary data associated with this article can be found in the online version at doi:10.1016/j.jallcom.2025.182503.

Data availability

The data of these findings can be shared by contacting the corresponding author.

References

[1] T.W. Penrice, Alternative binders for hard metals, Springe Verl. N. Y. Inc. (1987).

[2] H. Li, H. Zhang, Z. Jiang, Investigation of the effect of partial co substitution by Ni and Fe on the interface bond strength of WC cemented carbide based on first-principles calculations, Mater. Today Commun. 40 (2024), https://doi.org/10.1016/j.mtcomm.2024.109470.

[3] J. Sun, J. Zhao, F. Gong, X. Ni, Z. Li, Development and application of WC-based alloys bonded with alternative binder phase, Crit. Rev. Solid State Mater. Sci. 44 (2019) 211–238, https://doi.org/10.1080/10408436.2018.1483320.

[4] Z. Roulon, J.M. Missiaen, S. Lay, Carbide grain growth in cemented carbides sintered with alternative binders, Int. J. Refract Met. Hard Mater. 86 (2020), https://doi.org/10.1016/j.ijrmhm.2019.105088.

[5] E.M. Garcia-Ayala, L. Silvestroni, J. Yus, B. Ferrari, J.Y. Pastor, A.J. Sanchez-Herencia, Colloidal processing and sintering of WC-based ceramics with low Ni content as sintering aid, J. Eur. Ceram. Soc. 41 (2021) 1848–1858, https://doi.org/10.1016/j.jeurceramsoc.2020.10.038.

[6] D.D. Phuong, T.B. Trung, L.D. Chung, T.B. Hung, Effect of binder composition and sintering temperature on the microstructure and mechanical properties of WC-7 (Ni,Fe) hard alloys prepared by free capsule hip technique, Acta Metall. Slov. 25 (2019) 123–129, https://doi.org/10.12776/ams.v25i2.1270.

[7] S.H. Chang, S.L. Chen, Characterization and properties of sintered WC-Co and WC-Ni-Fe hard metal alloys, J. Alloy. Compd. 585 (2014) 407–413, https://doi.org/10.1016/j.jallcom.2013.09.188.

[8] O.O. Shichalin, I.Y. Buravlev, A.S. Portnyagin, M.I. Dvornik, E.A. Mikhailenko, A. V. Golub, A.M. Zakharenko, A.E. Sukhorada, K.Y. Talskikh, A.A. Buravleva, A. N. Fedorets, V.O. Glavinskaya, A.D. Nomerovskiy, E.K. Papynov, SPS hard metal alloy WC-8Ni-8Fe fabrication based on mechanochemical synthetic tungsten carbide powder, J. Alloy. Compd. 816 (2020), https://doi.org/10.1016/j.jallcom.2019.152547.

[9] Y. Gao, B.H. Luo, K. jian He, H. bo Jing, Z. hai Bai, W. Chen, W.W. Zhang, Mechanical properties and microstructure of WC-Fe-Ni-Co cemented carbides prepared by vacuum sintering, Vacuum 143 (2017) 271–282, https://doi.org/10.1016/j.vacuum.2017.06.028.

[10] Z. Zhao, J. Liu, H. Tang, X. Ma, W. Zhao, Effect of Mo addition on the microstructure and properties of WC-Ni-Fe hard alloys, J. Alloy. Compd. 646 (2015) 155–160, https://doi.org/10.1016/j.jallcom.2015.05.277.

[11] Y. Zheng, T. Huang, J. Yao, G. Fargas, E. Armelin, L. Llanes, C. Xie, D. Crespo, P. Bruna, O. Lavigne, Electrochemical corrosion behavior of WC-Co and WC-Ni cemented carbides: effect of chloride and sulfate ions, Int. J. Refract Met. Hard Mater. 132 (2025), https://doi.org/10.1016/j.ijrmhm.2025.107224.

[12] E.M. Garcia-Ayala, S. Tarancon, Z. Gonzalez, B. Ferrari, J.Y. Pastor, A.J. Sanchez-Herencia, Processing of WC/W composites for extreme environments by colloidal dispersion of powders and SPS sintering, Int. J. Refract Met. Hard Mater. 84 (2019), https://doi.org/10.1016/j.ijrmhm.2019.105026.

[13] E.M. Garcia-Ayala, S. Tarancon, B. Ferrari, J.Y. Pastor, A.J. Sanchez-Herencia, Thermomechanical behaviour of WC-W2C composites at first wall in fusion conditions, Int. J. Refract Met. Hard Mater. 98 (2021), https://doi.org/10.1016/j.ijrmhm.2021.105565.

[14] S.O. Nakonechnyi, A.I. Yurkova, P.I. Loboda, WC-based cemented carbide with NiFeCrWMo high-entropy alloy binder as an alternative to cobalt, Vacuum 222 (2024), https://doi.org/10.1016/j.vacuum.2024.113052.

[15] O. Urra, B. Ferrari, A.J. Sanchez-Herencia, G. Franchin, P. Colombo, Colloidal route towards sodium ionic conductor (NASICON) 3D complex solid electrolyte structures fabricated by direct ink writing (DIW), Open Ceram. 20 (2024), https://doi.org/10.1016/j.oceram.2024.100683.

[16] M. Biesuz, S. Grasso, V.M. Sglavo, What's new in ceramics sintering? A short report on the latest trends and future prospects, Curr. Opin. Solid State Mater. Sci. 24 (2020), https://doi.org/10.1016/j.cossms.2020.100868.

[17] A. Indurkar, R. Choudhary, K. Rubenis, J. Locs, Advances in sintering techniques for calcium phosphates ceramics, Materials 14 (2021), https://doi.org/10.3390/ma14206133.

[18] D.D. Phuong, P. Van Trinh, L. Van Duong, L.D. Chung, Influence of sintering temperature on microstructure and mechanical properties of WC-8Ni cemented carbide produced by vacuum sintering, Ceram. Int. 42 (2016) 14937–14943, https://doi.org/10.1016/j.ceramint.2016.06.134.

[19] S. Wen, Y. Du, Y. Liu, J. Tan, J. Long, M. Lou, K. Chang, L. Qiu, Z. Tan, L. Yin, G. Kaptay, Manipulation of the thermal conductivity for two-phase WC-Ni composites through a microstructure-based model along with key experiments, J. Mater. Res. Technol. 22 (2023) 895–912, https://doi.org/10.1016/j.jmrt.2022.11.136.

[20] R. Steinlechner, R. de Oro Calderon, T. Koch, P. Linhardt, W.D. Schubert, A study on WC-Ni cemented carbides: constitution, alloy compositions and properties, including corrosion behaviour, Int. J. Refract Met. Hard Mater. 103 (2022), https://doi.org/10.1016/j.ijrmhm.2021.105750.

[21] M.J.S. Lima, F.E.S. Silva, R.A. Raimundo, J.O. Vitoriano, C.S. Lourenço, M. Morales, M. Filgueira, U.U. Gomes, Enhanced properties of hard metal WC-Ni processed from nanostructured powders, Ceram. Int (2024), https://doi.org/10.1016/j.ceramint.2024.09.096.

[22] B. Roebuck, E.A. Almond, Deformation and fracture processes and the physical metallurgy of WC-Co hardmetals, 1988.

[23] S. Lay, HRTEM investigation of dislocation interactions in WC, Int. J. Refract Met. Hard Mater. 41 (2013) 416–421, https://doi.org/10.1016/j.ijrmhm.2013.05.017.

[24] X. Liu, J. Zhang, C. Hou, H. Wang, X. Song, Z. Nie, Mechanisms of WC plastic deformation in cemented carbide, Mater. Des. 150 (2018) 154–164, https://doi.org/10.1016/j.matdes.2018.04.025.

[25] H. Chen, H. Zhou, X. Cui, C. Czettl, T. Weirather, J. Pachlhofer, P. Mueller, T. Teppernegg, R. Useldinger, S. Primig, S.P. Ringer, Effect of WC/WC grain boundary misorientation angle on the local hardness in WC–Co cemented carbides, Scr. Mater. 259 (2025), https://doi.org/10.1016/j.scriptamat.2024.116525.

[26] M. Walbrühl, D. Linder, J. Ågren, A. Borgenstam, Alternative Ni-based cemented carbide binder – Hardness characterization by nano-indentation and focused ion beam, Int. J. Refract Met. Hard Mater. 73 (2018) 204–209, https://doi.org/10.1016/j.ijrmhm.2018.02.017.

[27] J.M. Tarragó, E. Jiménez-Piqué, L. Schneider, D. Casellas, Y. Torres, L. Llanes, FIB/FESEM experimental and analytical assessment of R-curve behavior of WC-Co cemented carbides, Mater. Sci. Eng. A 645 (2015) 142–149, https://doi.org/10.1016/j.msea.2015.07.090.

[28] E. Macarena García Ayala, A. Javier Sánchez Herencia, P.D. in Chemistry José Ygnacio Pastor Caño, Aqueous colloidal processing of W and WC-based composites, sintering and mechanical properties at high temperature, n.d.

[29] J. García, V. Collado Ciprés, A. Blomqvist, B. Kaplan, Cemented carbide microstructures: a review, Int J. Refract Met. Hard Mater. 80 (2019) 40–68, https://doi.org/10.1016/j.ijrmhm.2018.12.004.

[30] S. Fang, N. Salán, C. Pauly, L. Llanes, F. Mücklich, Critical assessment of two-dimensional methods for the microstructural characterization of cemented carbides, Metals 12 (2022), https://doi.org/10.3390/met12111882.

[31] J.C. WURST, J.A. NELSON, Lineal intercept technique for measuring grain size in two-phase polycrystalline ceramics, J. Am. Ceram. Soc. 55 (1972) 109–1019, https://doi.org/10.1111/j.1151-2916.1972.tb11224.x.

[32] V.T. Golovchan, N.V. Litoshenko, On the contiguity of carbide phase in WC-Co hardmetals, Int. J. Refract Met. Hard Mater. 21 (2003) 241–244, https://doi.org/10.1016/S0263-4368(03)00047-7.

[33] K.P. Mingard, B. Roebuck, Interlaboratory measurements of contiguity in wc-co hardmetals, Metals 9 (2019), https://doi.org/10.3390/met9030328.

[34] J.M. Tarragó, D. Coureaux, Y. Torres, F. Wu, I. Al-Dawery, L. Llanes, Implementation of an effective time-saving two-stage methodology for microstructural characterization of cemented carbides, Int J. Refract Met. Hard Mater. 55 (2016) 80–86, https://doi.org/10.1016/j.ijrmhm.2015.10.006.

[35] M. Pang, Y. Du, W.B. Zhang, Y.B. Peng, P. Zhou, A simplified hardness model for WC–co–cubic cemented carbides, J. Min. Metall. Sect. B Metall. 57 (2021) 253–259, https://doi.org/10.2298/JMMB200930021P.

[36] R. Astacio, M. Gallardo, J. Cintas, J.M. Montes, F.G. Cuevas, L. Prakash, Y. Torres, Fracture Toughness of Cemented Carbides Obtained by Electrical Resistance Sintering, n.d.

[37] A. Duthoit, E.J. Piqué, Advanced characterization techniques in cemented carbides Advanced Characterization Techniques in Cemented Carbides Report and Annex, n. d.

[38] C.M. Fernandes, A.M.R. Senos, Cemented carbide phase diagrams: a review, Int. J. Refract Met. Hard Mater. 29 (2011) 405–418, https://doi.org/10.1016/j.ijrmhm.2011.02.004.

[39] R.M. German, P. Suri, S.J. Park, Review: Liquid phase sintering, J. Mater. Sci. 44 (2009) 1–39, https://doi.org/10.1007/s10853-008-3008-0.

[40] P. Lu, R.M. German, Multiple grain growth events in liquid phase sintering, n.d.

[41] R. Warren, M.B. Waldront, Microstrijctural development during the I~Iquid-phase sintering of cemented carbides i. 'vettability and grain contact*, 1972.

[42] Y. Yuan, Z. Li, Growth mechanism of in-situ WC grain in Fe-Ni-W-C alloys system, J. Alloy. Compd. 738 (2018) 379–393, https://doi.org/10.1016/j.jallcom.2017.11.382.

[43] T. Nishi, S. Matsumoto, H. Yamano, K. Hayashi, R. Endo, M.R. Bellé, L. Neubert, O. Volkova, Density, surface tension, and viscosity of molten ni-based superalloys using the maximum bubble pressure and oscillating crucible methods, Steel Res Int (2024), https://doi.org/10.1002/srin.202300766.

[44] A. Salmasi, I. Hanif, T. Jonsson, H. Larsson, Liquid phase migration in cemented carbides – experiments and modelling, Int. J. Refract Met. Hard Mater. 112 (2023), https://doi.org/10.1016/j.ijrmhm.2023.106118.

[45] H. Wang, X. Kou, J. Zhang, J. Li, Large scale synthesis and characterization of Ni nanoparticles by solution reduction method, Bull. Mater. Sci. 31 (2008) 97–100, https://doi.org/10.1007/s12034-008-0017-1.

[46] J. Hodkiewicz, M. Wall, Introduction to Raman Spectroscopy as a Characterization Tool for Carbon Nanotubes, Graphene, and other Carbon Nanostructures, n.d. ⟨www.nsti.org⟩,.

[47] D.S. Knight, W.B. White, Characterization of diamond films by Raman spectroscopy, n.d. ⟨http://journals.cambridge.org⟩.

[48] D.R. Tallant, T.A. Friedmann, N.A. Missert, M.P. Siegal, J.P. Sullivan, Raman spectroscopy of amorphous carbon, Mater. Res. Soc. Symp Proc. (1997) 37–48, https://doi.org/10.1557/proc-498-37.

[49] A.C. Ferrari, Raman spectroscopy of graphene and graphite: disorder, electron-phonon coupling, doping and nonadiabatic effects, Solid State Commun. 143 (2007) 47–57, https://doi.org/10.1016/j.ssc.2007.03.052.

[50] A. Dychalska, P. Popielarski, W. Franków, K. Fabisiak, K. Paprocki, M. Szybowicz, Study of CVD diamond layers with amorphous carbon admixture by Raman scattering spectroscopy, Mater. Sci. Pol. 33 (2015) 799–805, https://doi.org/10.1515/msp-2015-0067.

[51] A.C. Ferrari, J.C. Meyer, V. Scardaci, C. Casiraghi, M. Lazzeri, F. Mauri, S. Piscanec, D. Jiang, K.S. Novoselov, S. Roth, A.K. Geim, Raman spectrum of graphene and graphene layers, Phys. Rev. Lett. 97 (2006), https://doi.org/10.1103/PhysRevLett.97.187401.

[52] A.A. Zegai, H. Besharatloo, P. Ortega, B. Djerdjare, B. Ferrari, A.J. Sanchez-Herencia, Microstructural and mechanical characterization of colloidal processed WC/(W5vol%Ni) via Spark plasma sintering, Materials 16 (2023), https://doi.org/10.3390/ma16134584.

[53] H. Rong, Z. Peng, X. Ren, Y. Peng, C. Wang, Z. Fu, L. Qi, H. Miao, Ultrafine WC-Ni cemented carbides fabricated by spark plasma sintering, Mater. Sci. Eng. A 532 (2012) 543–547, https://doi.org/10.1016/j.msea.2011.10.119.

[54] D. Kim, Y. Choi, Y. Kim, S. Jung, Characteristics of nanophase WC and WC-3 wt% (Ni, Co, and Fe) alloys using a rapid sintering process for the application of friction stir processing tools, Adv. Mater. Sci. Eng. 2015 (2015), https://doi.org/10.1155/2015/343619.

[55] E. Ghasali, T. Ebadzadeh, M. Alizadeh, M. Razavi, Mechanical and microstructural properties of WC-based cermets: A comparative study on the effect of Ni and Mo binder phases, Ceram. Int. 44 (2018) 2283–2291, https://doi.org/10.1016/j.ceramint.2017.10.189.

[56] A.V. Shatov, S.S. Ponomarev, S.A. Firstov, Fracture of WC-Ni cemented carbides with different shape of WC crystals, Int. J. Refract Met. Hard Mater. 26 (2008) 68–76, https://doi.org/10.1016/j.ijrmhm.2007.03.002.

[57] K.H. Shi, K.C. Zhou, Z.Y. Li, D. Zhang, X.Q. Zan, Microstructure and formation process of Ni-pool defect in WC-8Ni cemented carbides, Trans. Nonferrous Met. Soc. China 25 (2015) 873–878, https://doi.org/10.1016/S1003-6326(15)63676-7.